Structural and Optical Properties of Nanostructured Fe-Doped SnO₂

S.A. Saleh[a,b], A.A. Ibrahim[c] and S.H. Mohamed[a,*]

[a]Physics Department, Faculty of Science, Sohag University, Sohag 82524, Egypt

[b]Physics Department, College of Science and Arts, Najran University, P.O. 1988 Najran, KSA

[c]Chemistry Department, College of Science and Arts, Najran University, P.O. 1988 Najran, KSA

Nanocrystalline $Sn_{1-x}Fe_xO_2$ (where $x = 0$, 0.01, 0.02, 0.03 and 0.04) powders have been successfully synthesized by the hydrothermal method followed by sintering at $1000\,°C$ for 3 h. The morphology and structure of the samples have been analyzed by field emission scanning electron microscope and X-ray diffraction, respectively. X-ray diffraction results revealed that all diffraction peaks positions agree well with the reflection of a tetragonal rutile structure of SnO_2 phase without extra peaks. The formation of a tetragonal rutile structure of SnO_2 nanostructures was further supported by the Raman spectra. The band gap of Fe-doped SnO_2 nanoparticles was estimated from the diffuse reflectance spectra using the Kubelka–Munk function and it was decreasing slightly with the increase of Fe ion concentration from 3.59 to 3.52 eV. The variation in band gap is attributed predominantly to the lattice strain and particle size. The presence of chemical bonding was confirmed by the Fourier transform infrared spectra.

1. Introduction

In last over two decades nanoscale semiconducting oxides have significant interest due to their applications in sensing, optoelectronic devices, or catalysis [1]. These materials combining high optical transparency with good electrical conductivity have many different applications in contemporary and emerging technology such as in optoelectronic devices for emissive and nonemissive information display [2, 3].

Presently, significant attention is given to nanostructures made of SnO_2 and SnO_2-based optoelectronic materials because of the high transparency in the visible light range, high reflectance in the infrared (IR) region and high absorbance in the ultraviolet region and high electric conductivity besides the advantages of inorganic oxides such as high rigidity, excellent chemical inertness, etc. The coexistence of tin interstitials and oxygen vacancies in SnO_2 provide a unique combination of optical and electrical properties [4].

In view of its large number of applications, it is interesting to study and modify the properties of tin dioxide. Doping is widely used to modify properties of nanoscale semiconducting oxides; it offers the possibility of varying their lattice parameters, band gap, conductivity type, carrier concentration, and other properties [5]. Accordingly, it becomes important to understand the interplay between the nanoscale structure and optical properties of tin dioxide. This is essential for incorporating this system into technological applications that required tunable energy gaps including solar cells and optoelectronic devices [6]. Tuning the optical properties by controlling the band gap is a great challenge since attention should also be directed to avoid the interfacial defects and stress which may occur due to lattice mismatches between the two materials [7].

Noteworthy, the crystal structure of SnO_2 plays an important role in its optoelectronic performance. Furthermore, the optical transparency in the visible region together with electronic conductivity is accomplished by introducing nonstoichiometry and/or appropriate dopants in wide band-gap oxides. Of course, optimal operational performance requires materials with well-defined physical parameters that can be modified and tuned by doping with suitable foreign atoms. It is well known that the introduction of dopants not only results in interesting new effects but also presents, on occasion, an opportunity to acquire knowledge of the host material itself which would be almost impossible to obtain otherwise. Moreover, SnO_2, one of the first transparent conductors [8], is a degenerate n-type semiconductor because of intrinsic defects (O vacancies or Sn interstitials) [9–12] and its properties can be highly tailored with suitable dopant elements. Many results have shown that several dopants (Co, Fe, and Cu) can lead to an increase of surface area of SnO_2 by reducing the grain size and crystallinity [13–15]. Thus, the final properties of impurity doped SnO_2 nanoparticles are related to both composition and processing method.

It is known that the optoelectronic properties of nanoparticles sensitively depend on their shapes and size that are mainly determined by the physico-chemical parameters of the synthesis method. Among the synthetic

---

*corresponding author; e-mail: abo_95@yahoo.com

techniques, hydrothermal route [16] is much preferred for its simplicity and controllability of grain size, morphology and degree of crystallinity by changing the experimental parameters [17]. Moreover, it has been recognized as an environmentally friendly process because it uses water as a reaction medium and reaction is carried out in an autoclave, which is an enclosed system [18–21].

In this study, a very simple and efficient method for the synthesis of SnO$_2$ nanoparticles is described. The effect of Fe concentration on various structural, morphological and optical properties of SnO$_2$ nanoparticles was studied. The Raman spectroscopy in addition to the X-ray diffraction (XRD) and field emission scanning electron microscopy (FESEM) were used to study the structure of pure and doped SnO$_2$ nanostructure while UV-Visible and the Fourier transform infrared (FTIR) spectrophotometry were used for optical studies.

2. Experimental details

All the chemicals utilized for the synthesis of SnO$_2$ and Fe-doped SnO$_2$ were purchased from Sigma-Aldrich and used without further purifications. Well-crystalline SnO$_2$ was prepared using a conventional hydrothermal method using tin nitrate Sn(NO$_3$)$_2$ (0.1 M) in 100 ml of deionized water under continuous stirring for one hour. After stirring, few drops of ammonium hydroxide (NH$_4$OH) were added in the resultant solution to maintain the pH at 10. The final solution was vigorously stirred for one hour again and consequently transferred to teflon lined autoclave, sealed and heated up to 130 °C for 8 h. After that time, the autoclave was allowed to cool at room temperature. Finally, a white precipitate was obtained which was washed extensively several times with ethanol, deionized water and acetone, sequentially and dried at room temperature. The dried powder was calcinated for 3 h at 1000 °C with gradual elevation of temperature, then characterized in detail in terms of their morphological, structural, compositional and optical properties. To synthesize the Fe-doped SnO$_2$, we repeated the above process with adding Fe(NO$_3$)$_3$ · 6H$_2$O at different concentrations (0.01–0.04 M) to obtain 1%, 2%, 3%, and 4% Fe-doped SnO$_2$.

Powder XRD patterns of the prepared samples were taken by a two-circle ($2\theta - \theta$) X-ray powder diffractometer (PANalytical X'PertPRO) at room temperature using Cu K_α radiation ($\lambda = 0.15406$ nm). The scan was taken between 2θ of 20° and 2θ of 80° at increments of 0.02° with a count time of 4 second for each step. The morphology and microstructure were examined using FESEM (JEOL JSM-7600F). Elemental analysis of the prepared samples was performed by taking a spectrum of energy dispersive spectroscopy (EDS) attached to the FESEM. Raman spectra of the samples were recorded at room temperature with Perkin Elmer (Raman station 400) Raman spectrometer in the wave number region 1000–100 cm^{-1} at 4 cm^{-1}. The resolution and excitation wavelengths were provided by an Ar$^+$ Spectra-Physics Laser with exciting wavelength of 514.5 nm. Room temperature diffusion reflection spectra were recorded on

a UV–Vis spectroscopy (Perkin Elmer's LAMBDA 950 spectrophotometer) through the Kubelka–Munk function. The presence of functional groups in nanoparticles were analyzed by FTIR spectrometer (Model: Spectrum-100: Perkin Elmer) in the wave number ranges from 400 to 4000 cm^{-1}. The samples used for this measurement are in the form of pellets prepared by mixing the nanoparticles with KBr at 1 wt%.

3. Results and discussions

The morphologies and microstructures of the pure and Fe-doped SnO$_2$ powders were characterized by FESEM. Representative FESEM images of undoped and Fe-doped SnO$_2$ samples were depicted in Fig. 1. The data imply that the synthesized samples are composed of uniformly distributed particles of almost similar size. The average size of the particles decreases markedly as the Fe doping level increases suggesting that Fe plays vital role in the growth inhibition of the SnO$_2$ material. This can be attributed to the increased nucleation sites resulted from higher stacking fault energy due to Fe incorporation in the SnO$_2$ material [22].
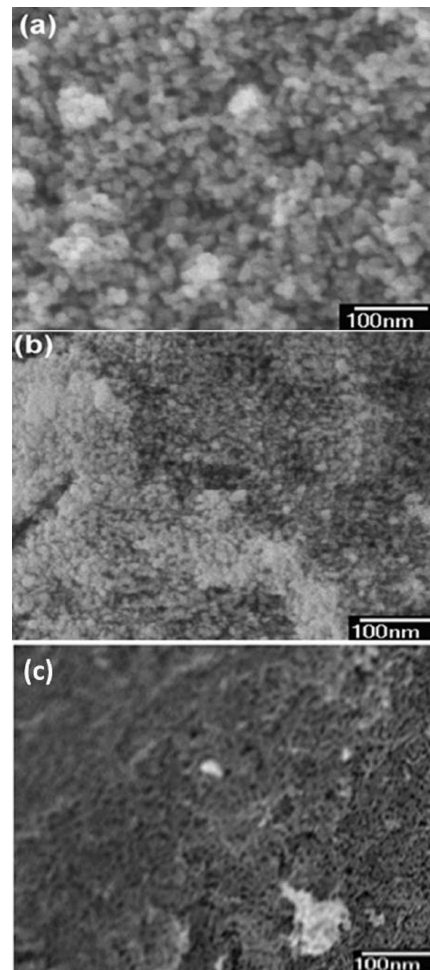

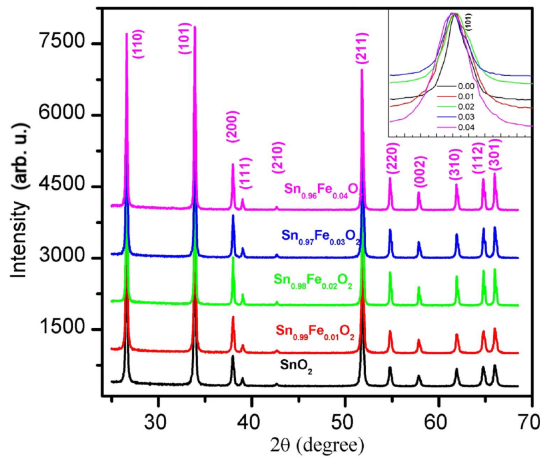Fig. 1. FESEM images of (a) 0%, (b) 1% Fe, and (c) 2% Fe.

Fig. 2. X-ray diffraction patterns of $Sn_{1-x}Fe_xO_2$ with various Fe concentrations.

XRD analysis was carried out to identify the crystal structure and phase purity of the samples. The indexing of XRD patterns presented in Fig. 2 revealed that the structure is typical for the tetragonal rutile structure of the cassiterite SnO_2 phase with space group $P4_2/mnm$ (136) (JCPDS file no. 41-1445). No alien phases have been observed confirming that SnO_2 with tetragonal cassiterite structure is the only crystalline phase appearing in both undoped and Fe-doped SnO_2 nanoparticles.

The mean grain size D of the Fe^{3+}-doped SnO_2 nanoparticles was calculated from (101) peak (see inset of Fig. 2) using the Scherrer equation

$$D = \frac{0.89\lambda}{\beta \cos \theta}, \tag{1}$$

where λ, β and θ are the X-ray wavelength, the full width at half-maximum (FWHM) of the most intense peak in radians and the Bragg angle, respectively. The calculations show that the Fe-doping makes effects on the size of the nanoparticles where nanoparticles' diameter decreases from 26.7 to 17.9 nm as the Fe^{3+} content increases from 0.0 to 4%. Moreover, it can be noted that doping SnO_2 with Fe^{3+} can hinder the grain growth as well, and this supports the observance of decreasing crystallite sizes [23, 24].

The Raman spectroscopy is a useful tool for characterization of nanosized materials and can be used as a qualitative probe to estimate the presence of lattice defects in crystalline solids. The crystalline quality can be judged from the analysis of the peak shapes and the selection rules. Tetragonal rutile SnO_2 belongs to the space group D_{4h}^{14} and based on the group theory, the following optical phonons at the Γ point of the Brillouin zone can be presented:

$$\Gamma = 1A_{1g} + 1A_{2g} + 1A_{2u} + 1B_{1g} + 1B_{2g}$$

$$+2B_{1u} + 1E_g + 3E_u. \tag{2}$$

The four modes (three non-degenerate modes A_{1g}, B_{1g}, B_{2g} and doubly degenerate E_g) are the Raman

active while two modes (A_{2u} and triply degenerate E_u) are IR active. On the other hand, the two modes of A_{2g} and B_{1u} are silent modes. The A_{1g}, B_{1g}, and B_{2g} modes arising due to the vibration of oxygen atom with the plane perpendicular to c axis, while E_g is due to vibration in the direction of the c axis [25, 26]. The Raman spectra of undoped and Fe-doped SnO_2 samples recorded in the frequency range 100–1000 cm^{-1} are presented in Fig. 3. The pure SnO_2 shows three prominent Raman peaks at 474, 632 and 772 cm^{-1} which are assigned to E_g, A_{1g} and B_{2g} modes, respectively [27, 28]. As Fe concentration increased some extra peaks are observed at 220, 287, 405, 472 and 490 cm^{-1}. The observation of these new peaks can be explained on the basis of the nano effect associated with Fe doping.
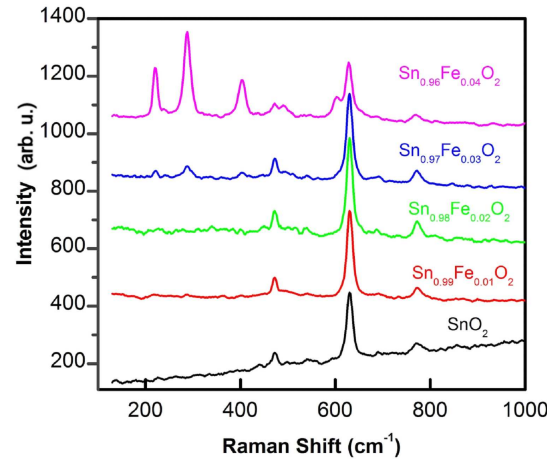

Fig. 3. Raman spectra of nanocrystalline SnO_2 doped with Fe.

In nanocrystalline SnO_2 system, the surface properties are sensitive not only to the grain size and their distributions but also the oxygen vacancies and local disorder so there may be possibility of the appearance of new modes in the Raman spectra [29]. It is also interesting to note that by substituting Fe in the SnO_2 lattice, the intensities of the three main Raman peaks are found to decrease. This behavior might be due to the fact that the dopants Fe substitution might be responsible for the changes in local disorder and defects such as vacant lattice sites or vacancy cluster or local disorder which may result in lattice distortion and reduction in lattice space symmetry. The absence of the known crystalline phases of Fe_2O_3 in the doped samples (as revealed by XRD analysis) suggests that it is finely dispersed in SnO_2 matrix.

Diffuse reflectance spectroscopy is an excellent diagnostic tool for optical characterization of powdered, crystalline and nanostructure materials in different spectral ranges. It provides useful information about the optical band gap of the semiconductors. To determine the optical band-gap of synthesized Fe-doped SnO_2 nanopowders, the ultraviolet-visible diffuse reflectance spectra of pure and Fe-doped SnO_2 nanopowders are measured at
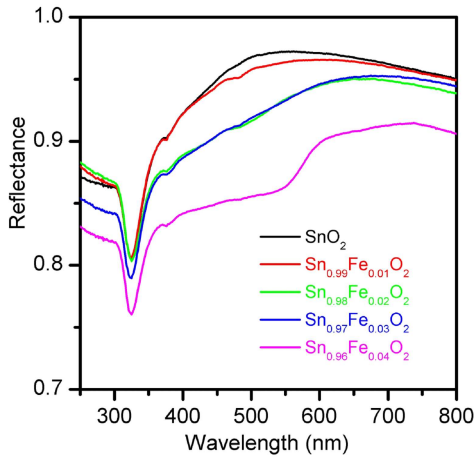
Fig. 4. Room temperature UV-Vis diffused reflectance spectra of Fe doped SnO$_2$ samples as a function of wavelength.

room temperature. The UV-Vis diffused reflectance spectra of the undoped and Fe-doped SnO$_2$ as a function of wavelengths are shown in Fig. 4. Obviously, the reflectance spectra show a strong decrease at absorption edge. This decrease is related to optical transitions occurring in the optical band-gap.

In order to determine the precise value of the optical band-gap of the Sn$_{1-x}$Fe$_x$O$_2$, the reflectance values were converted to absorbance by applying the Kubelka–Munk (KM) function [30, 31]. The KM theory is generally used for analyzing the diffuse reflectance spectra obtained from weakly absorbing samples. In this case, the KM formula at any wavelength becomes [32]:

$$F(R) = \frac{(1-R)^2}{2R}, \tag{3}$$

where $F(R)$ is the KM function which is proportional to the absorption coefficient (α). It is well known that the optical transitions in semiconductor materials take place by direct and indirect transitions. The absorption coefficient α of an indirect/direct semiconductor near the absorption threshold can be expressed by the following relation [33]:

$$\alpha = \frac{\beta \left(h\nu - E_g^{opt} \right)^n}{h\nu}, \tag{4}$$

where E_g^{opt} is the band gap (eV) of indirect allowed transition for $n = 2$ and of direct allowed transition for $n = \frac{1}{2}$, h is the Planck constant in J s, β is the absorption constant, and ν is the frequency of the light (s^{-1}). In the present case, $n = \frac{1}{2} n = \frac{1}{2}$ that is for direct allowed transition. The intercept of the plot between $[F(R) * h\nu]^2$ versus $h\nu$ gives the optical band gap energy (see Fig. 5). By extrapolating the linear portions of these plots to the photon energy axis, values of the optical band gap for pure and Fe-doped SnO$_2$ are obtained. The obtained E_g^{opt} values are 3.59, 3.58, 3.56, 3.55, and 3.52 eV, for Fe concentrations of 0, 0.01, 0.02, 0.03 and 0.04, respectively. It is therefore clear that the Fe doped samples

have slightly less band gap energy than undoped SnO$_2$ samples. This decrease may be ascribed to the accumulation of donor energy levels of transition Fe ions in the actual band gap of SnO$_2$ [34], besides the strain which could be initiated in the samples during preparation [35]. Such a decrease in E_g^{opt} has been reported previously for Ni and Fe doped SnO$_2$ thin films [34, 36] and was ascribed to the existence of Ni or Fe at the cation site in the SnO$_2$ host matrix. Similarly, the Fe ions may expect to exist at Sn sites of SnO$_2$ lattice thereby causes the detected band gap narrowing.
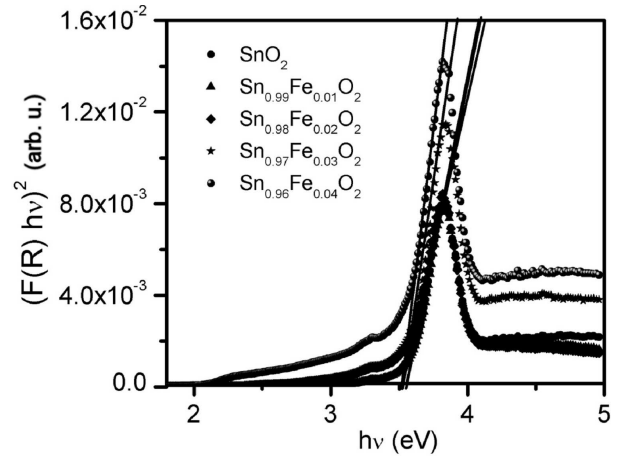

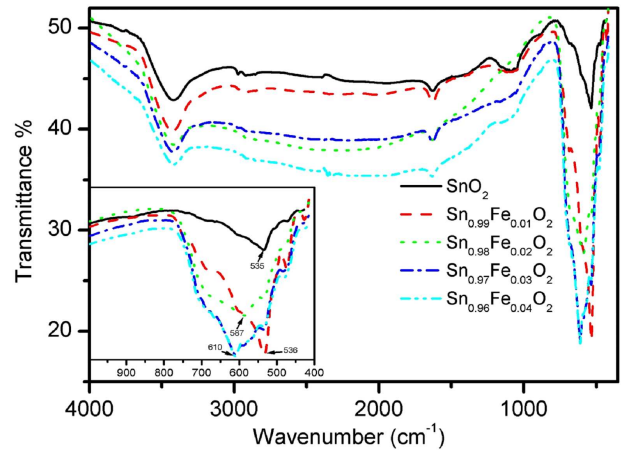Fig. 5. $(F(R) * h\nu)^2$ versus $h\nu$ plots.

Fig. 6. FTIR analysis of pure and Fe doped SnO$_2$ nanoparticles.

FTIR is a technique used to obtain information regarding chemical bonding and functional groups in a material. In the transmission mode, it is quite useful to predict the presence of certain functional groups which are adsorbed at certain frequencies, thus, it reveals the structure of the material. The band positions and numbers of absorption peaks depend on the crystalline structure, chemical composition, and also on morphology [37]. In the nanoscale materials, the surface is highly sensitive and greatly modified easily. To investigate chemical groups on the surface

of sintered samples, an FTIR analysis was carried out at room temperature over the wave number range of 400–4000 cm^{-1}. The FTIR transmittance spectra of all the Fe:SnO$_2$ nanoparticles sintered at 1000 °C for 3 h are presented in Fig. 6. There are several bands appearing in the wave number range 400–4000 cm^{-1}. The broad absorption band at 3423 cm^{-1}, the peaks at 2977 cm^{-1}, and 1630 cm^{-1} are assigned to the vibration of hydroxyl group due to the absorbed/adsorbed water and show a stretching vibrational mode of O–H group [38]. Absorption peaks observed around 2380 cm^{-1} belong to the stretching vibrations of C–H bonds that could be due to the adsorption and interaction of atmospheric carbon dioxide with water during the sintering process [39]. The bands observed in the range of 970–700 cm^{-1} are due to the vibration of Sn=O and Sn–O surface cation-oxygen bonds [38]. The very strong absorption bands observed in the range of 420–700 cm^{-1} are attributed to the Sn–O antisymmetric vibrations. In that region, the peak at 686 cm^{-1} are assigned to Sn–O–Sn vibrations, respectively [34]. The bands exhibited in the low wave number region 430–620 cm^{-1} are attributed to the Sn–O stretching vibrations [40]. The Fe doping shifts the positions of the absorption bands (see the inset of Fig. 6). It has been previously reported that changes observed in the shape, width, and positions of FTIR peaks are attributed to the variation in the local defects, grain size and shape of the nanoparticles [41]. In all samples, the vibrations associated to C–H and O–H bonds are seen. This implies that the surface is highly active and adsorbed these molecules.

4. Conclusions

In this paper we have successfully synthesized (0%, 1%, 2%, 3%, and 4%) Fe doped SnO$_2$ nanoparticles using hydrothermal method. The FESEM study showed that the Fe doping reduced the average crystal size by preventing subsequent growth of the grain surface. The tetragonal structure of all prepared samples was confirmed by X-ray diffraction spectra and the Raman scattering. The changes in average crystal size, peak position shift and peak intensity confirmed the Fe substitution in SnO$_2$ lattice. Evolution of the Raman spectra reveals the formation of SnO$_2$ structure in each sample and existence of nanosize particles. FTIR analysis revealed that the Fe doping manifests itself by a shift in Sn–O absorption peaks positions. For optical studies, the dependence of Fe concentrations on the optical band gap was elucidated. The optical band gap decreased slightly with increase in Fe concentrations.

References

[1] L. Diamandescu, D. Tarabasanu-Mihaila, M. Feder, M. Enculescu, V.S. Teodorescu, S. Constantinescu, T. Popescu, C. Bartha, Zs. Pap, *Mater. Chem. Phys.* **143**, 1540 (2014).

[2] D.-W. Kim, I.-S. Hwang, S.J. Kwon, H.-Y. Kang, K.-S. Park, Y.-J. Choi, K.-J. Choi, J.-G. Park, *Nanoletters* **7**, 3041 (2007).

[3] J.Q. Hu, Y. Bando, Q.L. Liu, D. Golberg, *Adv. Funct. Mater.* **13**, 493 (2003).

[4] M.M. Rahman, S.B. Khan, A. Jamal, M. Faisal, A.M. Asiri, *Talanta* **95**, 18 (2012).

[5] J. Mazloom, F.E. Ghodsi, H. Golmojdeh, *J. Alloys Comp.* **639**, 393 (2015).

[6] M.B. Sahana, C. Sudakar, G. Setzler, A. Dixit, J.S. Takur, G. Lawes, R. Naik, V.M. Naik, P.P. Vaishnava, *Appl. Phys. Lett.* **93**, 231909 (2008).

[7] C.J. Murphy, J.L. Coffer, *Appl. Spectrosc.* **56**, 16A (2002).

[8] G. Turgut, E.F. Keskenler, S. Aydın, D. Tatar, E. Sonmez, S. Dogan, B. Duzgun, *Rare Met.* **33**, 433 (2014).

[9] A.V. Moholkar, S.M. Pawar, K.Y. Rajpure, P.S. Patil, C.H. Bhosale, *J. Phys. Chem. Solids* **68**, 1981 (2007).

[10] M. Batzill, U. Diebold, *Prog. Surf. Sci.* **79**, 47 (2005).

[11] C. Kılıç, A. Zunger, *Phys. Rev. Lett.* **88**, 095501 (2002).

[12] K. Ravichandran, K. Thirumurugan, *J. Mater. Sci. Technol.* **30**, 97 (2014).

[13] H. Jin, Y. Xu, G. Pang, W. Dong, Q. Wan, Y. Sun, S. Feng, *Mater. Chem. Phys.* **85**, 58 (2004).

[14] J. Hays, A. Punnoose, R. Baldner, M.H. Engelhard, J. Peloquin, K.M. Reddy, *Phys. Rev. B* **72**, 075203 (2005).

[15] G. Korotcenkov, V. Macsanov, V. Brinzari, V. Tolstoy, J. Schwank, A. Cornet, J. Morante, *Thin Solid Films* **467**, 209 (2004).

[16] H. Zhu, D. Yang, G. Yu, H. Zhang, K. Yao, *Nanotechnology* **17**, 2386 (2006).

[17] B.M. Matin, Y. Mortazavi, A.A. Khodadadi, A. Abbasi, A.A. Firooz, *Sens. Actuat. B* **151**, 140 (2010).

[18] A. Kawai-Nakamura, T. Sato, K. Sue, S. Tanaka, K. Saitoh, K. Aida, T. Hiak, *Mater. Lett.* **62**, 3471 (2008).

[19] C. Lazau, L. Mocanu, I. Miron, P. Sfirloaga, G. Tanasie, C. Tatu, A. Gruia, I. Grozescu, *Digest J. Nanomater. Biostruct.* **2**, 257 (2007).

[20] K.M. Reddy, D. Guin, S.V. Manorama, A.R. Reddy, *J. Mater. Res.* **19**, 2567 (2004).

[21] H. Zhang, N. Du, B. Chen, T. Cui, D. Yang, *Mater. Res. Bull.* **43**, 3164 (2008).

[22] M.V. Vaishampayan, R.G. Deshmukh, P. Walke, I.S. Mulla, *Mater. Chem. Phys.* **109**, 230 (2008).

[23] S. Rani, S.C. Roy, M.C. Bhatnagar, *Sens. Actuat. B* **122**, 204 (2007).

[24] T.N. Soitah, C. Yang, L. Sun, *Mater. Sci. Semicond. Proc.* **13**, 125 (2010).

[25] A. Diéguez, A. Romano-Rodríguez, A. Vilà, J.R. Morante, *J. Appl. Phys.* **90**, 1550 (2001).

[26] X. Mathew, J.P. Enriquez, C. Mejía-García, G. Contreras-Puente, M.A. Cortes-Jacome, J.A.T. Antonio, J. Hays, A. Punnoose, *J. Appl. Phys.* **100**, 073907 (2006).

[27] P.S. Peercy, B. Morosin, *Phys. Rev. B* **7**, 2779 (1973).

[28] S.K. Pillai, L.M. Sikhwivhilu, T.K. Hillie, *Mater. Chem. Phys.* **120**, 619 (2010).

[29] J. Kaur, J. Shah, R.K. Kotnala, K.C. Verma, *Ceram. Int.* **38**, 5563 (2012).

[30] C. Aydın, M.S. Abd El-sadek, K. Zheng, I.S. Yahia, F. Yakuphanoglu, *Opt. Laser Technol.* **48**, 447 (2013).

[31] G.E. Patil, D.D. Kajale, V.B. Gaikwad, G.H. Jain, *Int. Nano Lett.* **2**, 17 (2012).

[32] V. Senthilkumar, K. Senthil, P. Vickraman, *Mater. Res. Bull.* **47**, 1051 (2012).

[33] R. López, R. Gómez, *J. Sol-Gel Sci. Technol.* **61**, 1 (2012).

[34] A. Sharma, M. Varshney, S. Kumar, K.D. Verma, R. Kumar, *Nanomater. Nanotechnol.* **1**, 29 (2011).

[35] B. Nandan, B. Venugopal, S. Amirthapandian, B.K. Panigrahi, P. Thangadurai, *J. Nanopart. Res.* **15**, 1999 (2013).

[36] T.N. Soitah, C. Yang, L. Sun, *Mater. Sci. Semicond. Proc.* **13**, 125 (2010).

[37] M. Ashokkumar, S. Muthukumaran, *Superlatt. Microstruct.* **69**, 53 (2014).

[38] M. Faisal, A.A. Ibrahim, F.A. Harraz, H. Bouzid, M.S. Al-Assiri, A.A. Ismail, *J. Mol. Cat. A Chem.* **397**, 19 (2015).

[39] S. Gnanam, V. Rajendran, *J. Sol-Gel Sci. Technol.* **56**, 128 (2010).

[40] S.H. Mohamed, *J. Alloys Comp.* **510**, 119 (2012).

[41] K. Srinivas, S.M. Rao, P.V. Reddy, *Nanoscale* **3**, 642 (2011).